PCCP

PAPER

View Article Online
View Journal | View Issue

Cite this: *Phys. Chem. Chem. Phys.*, 2017, **19**, 5361

Valence band dispersion measurements of perovskite single crystals using angle-resolved photoemission spectroscopy†

Congcong Wang,[a] Benjamin R. Ecker,[a] Haotong Wei,[b] Jinsong Huang,[b] Jian-Qiao Meng[c] and Yongli Gao*[a]

Received 19th October 2016,
Accepted 11th January 2017

DOI: 10.1039/c6cp07176g

rsc.li/pccp

The electronic structure of a cleaved perovskite ($CH_3NH_3PbBr_3$) single crystal was studied in an ultra-high vacuum (UHV) system using angle-resolved photoemission spectroscopy (ARPES) and inverse photoelectron spectroscopy (IPES). Highly reproducible dispersive features of the valence bands were observed with symmetry about the Brillouin zone center and boundaries. The largest dispersion width was found to be $\sim$0.73 eV and $\sim$0.98 eV along the ΓX and ΓM directions, respectively. The effective mass of the holes was estimated to be $\sim 0.59 m_0$. The quality of the surface was verified using atomic force microscopy (AFM) and scanning electron microscopy (SEM). The elemental composition was investigated using high resolution X-ray photoelectron spectroscopy (XPS). The experimental electronic structure shows a good agreement with the theoretical calculation.

Introduction

Hybrid organic–inorganic halide perovskites have first attracted intense attention for their potential applications in high-performance photovoltaic devices.[1–5] After only a few years of active research, the power conversion efficiency of the devices has reached 22.1%.[6] More importantly, the use of halide perovskites has expanded beyond just photovoltaic devices to a variety of other equally important applications such as photodetectors,[5] light emitting diodes (LEDs)[7] and lasers.[8] While the material growth processes,[9–12] electronic density of states[13–15] and the stability[16–18] have been widely studied, the underlying intrinsic carrier transport properties of the materials remain poorly understood. They have so far been limited to either theoretical modelling[19] or indirectly acquisition[20] from transistors made from polycrystalline films where real intrinsic properties could be masked. Indeed for every application listed above, such a characteristic is the key to a fundamental understanding and prediction of the actual device performance.

Studies of band structures are very important for understanding their electronic properties and transport characteristics. Theoretical calculations and combined experimental studies have been performed to investigate the band structure of perovskite,[21–28] yet few direct measurements of band dispersion, effective mass and hole mobility determining its transport characteristics have been made. Angle-resolved photoemission spectroscopy (ARPES) is an ideal technique to directly determine the band structure. To focus on the intrinsic carrier dynamics, freshly cleaved single crystals have been used to reduce any possible extrinsic factors, such as impurities and grain boundaries.

In this manuscript, we report our investigation on the band dispersion of a high quality $CH_3NH_3PbBr_3$ single crystal using ARPES. The band widths were measured to be 0.73 and 0.98 eV along ΓX and ΓM, respectively. Together with inverse photoelectron spectroscopy (IPES), the band gap was measured to be 2.3 eV. The slight n-type crystal was cleaved in an ultra-high vacuum (UHV) system and the composition was investigated using high resolution X-ray photoelectron spectroscopy (XPS). The quality of the surface was investigated by atomic force microscopy (AFM) and scanning electron microscopy (SEM).

Experimental

Sample preparation

The high quality methylammonium lead bromide perovskite single crystals were synthesized by a solution-processed anti-solvent growth method as described in ref. 5. Briefly, 0.64 M $PbBr_2$ and 0.8 M methylamine bromine were dissolved in 5 ml of *N*,*N*-dimethylformamide solution in a small vial. Then the vial was

[a] *Department of Physics and Astronomy, University of Rochester, Rochester, NY 14627, USA. E-mail: ygao@pas.rochester.edu*
[b] *Department of Mechanical and Materials Engineering, University of Nebraska-Lincoln, Lincoln, Nebraska 68588, USA*
[c] *Hunan Key Laboratory of Super-microstructure and Ultrafast Process, School of Physics and Electronics, Central South University, Changsha, Hunan 410083, P. R. China*

† Electronic supplementary information (ESI) available. See DOI: 10.1039/c6cp07176g

sealed with foil, but leaving a small hole to let dichloromethane slowly get in. Dichloromethane was employed as the anti-solvent to precipitate the single crystals. Finally, the vial was stored in the atmosphere of dichloromethane, and $CH_3NH_3PbBr_3$ single crystals slowly grew in two days. Each experiment was performed on a freshly cleaved sample at room temperature. In particular for ARPES, IPES and XPS measurements, the crystals were cleaved in an UHV system (*in situ*). For AFM, SEM and energy dispersive spectroscopy (EDS) measurements, the samples were cleaved *ex situ*. The detailed cleavage process is described in the ESI† (Fig. S1). The average size of the crystals is ~6 mm × 6 mm × 3.5 mm.

Characterization

The morphology and the initial elemental analysis of the as-cleaved sample were obtained by using an NTMDT AFM and a Zeiss Auriga SEM with a built-in EDS system. Powder XRD measurements were performed using a Rigaku D/Max-B X-ray diffractometer with Bragg–Brentano parafocusing geometry, a diffracted beam monochromator, and a conventional cobalt target X-ray tube set to 40 kV and 30 mA.

Photoelectron spectroscopy measurements

The ARPES measurements were performed on the perovskite single crystal (001) surface using a VG ESCA Lab UHV system equipped with a He I (21.2 eV) gas discharge lamp. The base pressure of the spectrometer chamber is typically 8×10^{-11} Torr. The typical instrumental energy resolution for ultraviolet photoelectron spectroscopy (UPS) measurements ranges from ~0.03 to 0.2 eV with a photon energy dispersion of less than 20 meV. The UV light spot size on the sample is about 1 mm in diameter. The detector angular resolution is ~0.5°. The surface composition information was measured using a high resolution XPS with a monochromatic Al Kα source (1486.6 eV) in an UHV chamber with a base pressure of 1×10^{-10} Torr. The energy resolution of XPS is about 0.6 eV. The X-ray spot size on the sample is about 0.1 mm in diameter. The IPES spectra were recorded using a custom-made spectrometer, composed of a commercial Kimball Physics ELG-2 electron gun and a band pass photon detector. The photon detector was operated in the isochromatic mode centered at a fixed energy of 9.8 eV. The combined resolution (electron and photon) of the IPES spectrometer was determined to be ~0.6 eV.

Results and discussion

Fig. 1a shows the as-grown perovskite single crystal (001) surface with an average area of 6 mm × 6 mm. The thickness of the sample is ~3.5 mm. Powder XRD of the ground crystal confirmed the cubic crystal structure of the sample (Fig. S2, ESI†). The reciprocal lattice of the crystal unit cell is shown in Fig. 1b, where ΓX, ΓY, and ΓM directions correspond to the *a*-axis, the *b*-axis (Fig. 1a) and the face diagonal direction, respectively. The ΓR direction could not be evaluated because of the limitation of the intrinsic (001) cleavage plane of the perovskite material. Due to the crystal symmetry, ΓX, ΓY and ΓZ directions are all degenerate. Therefore, later ARPES measurements were only performed along the ΓX and ΓM directions. The three-dimensional

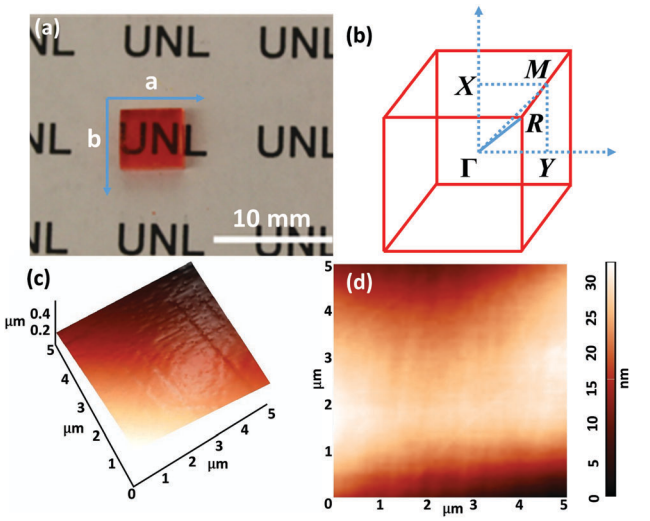

Fig. 1 (a) $CH_3NH_3PbBr_3$ single crystal with a surface area of 6 mm × 6 mm. (b) The reciprocal lattice of cubic $CH_3NH_3PbBr_3$. Three-dimensional (3D) (c) and 2D (d) AFM images of the crystal surface in two test areas (5 μm × 5 μm).

(3D) and two-dimensional (2D) AFM images were taken at three different locations (Fig. 1c, d and Fig. S3, ESI†) to illustrate the high quality of the surface, which is a prerequisite for achieving accurate band structure results from ARPES. The average root mean square (RMS) roughness of the three positions is as low as 4.273 nm, indicating a very smooth surface. The surface quality was also imaged by SEM, and the built-in EDS system confirmed the existence of Pb and Br (Fig. S4, ESI†).

Fig. 2a shows the high resolution XPS survey scan of the perovskite single crystal. The detailed photoelectron spectroscopy figures for individual elements could be found in Fig. S5 (ESI†). The composition of the as-cleaved sample is C : N : Pb : Br : O = 1.46 : 1.05 : 1.02 : 3.04 : 0.05, if Pb 4f from perovskite is taken as the basis (the extra 0.02 Pb 4f is metal lead). This ratio is very close to the ideal value. The excessive carbon, nitrogen, bromine, and oxygen may have come from residual reactants used during the crystal growth process. The detailed analysis is shown in Table S1 (ESI†). Another possible explanation is that the cleavages were done along an impurity rich region (where a fracture is easier to take place), but the bulk of the crystal still follows the stoichiometric ratio.

Fig. 2b shows the bandgap diagram of the sample measured by UPS and IPES. It shows the binding energy (BE) from the Fermi level (E_F) of the material. For visual clarity, we normalized all the spectra to the same height. The cut-off energy is determined by the inflection point of the sharp change region of the cut-off spectrum.[29–31] The vacuum level (VL) is obtained from the difference between the photon energy (21.22 eV) and the cut-off energy. The VL of the $CH_3NH_3PbBr_3$ single crystal is measured to be 4.61 eV above the E_F, *i.e.* the work function (WF). In the highest VB lying regions, the valence band maximum (VBM) of the single crystal displays ~1.49 eV. To obtain the detailed information on the unoccupied states of perovskite single crystals, we further collected the IPES data. The conduction band minimum (CBM) is measured to be ~0.81 eV above the E_F, while the VBM is ~1.49 eV below the E_F,

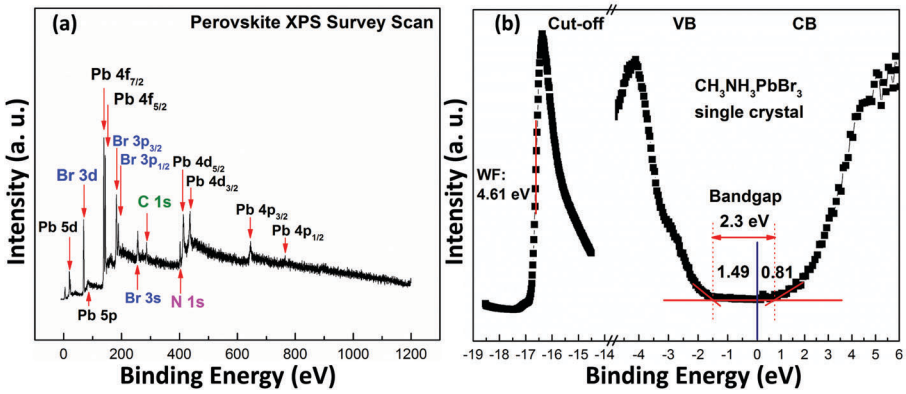

Fig. 2 (a) High resolution XPS survey scan and (b) bandgap diagram of the $CH_3NH_3PbBr_3$ single crystal.

corresponding to a bandgap of 2.3 eV that is consistent with previous reports.[32,33] The valence band (VB) and conduction band (CB) edges are obtained using linear extrapolation as illustrated in our previous study.[34] The ionization potential (energy of the VBM referenced to the VL) is 6.10 eV. The crystal surface presents a slight n-type semiconductor behavior. The indirect character of the bandgap as discussed for $CH_3NH_3PbI_3$ thin films[35] was not observed for the $CH_3NH_3PbBr_3$ single crystal.

In Fig. 3a and b, we present angle-resolved energy distribution curves (EDCs) of the overall valence band as a function of electron emission angle θ relative to the surface normal measured along ΓX and ΓM directions, respectively. All the spectra were normalized to the same height and fitted by four Gaussian peaks, VB-A, VB-B, VB-C, and VB-D. One detailed analysis is shown in the inset of Fig. 3a. Both series of spectra show a structured and angle-dependent valence-band emission. For both the ΓX and ΓM directions, as θ increases, all the peaks shift towards a higher BE until they reached the Γ point (0°). After passing through the Γ point, the peaks show an upward dispersion and reach the minima at around 16.5° and 22.5° in ΓX and ΓM directions,

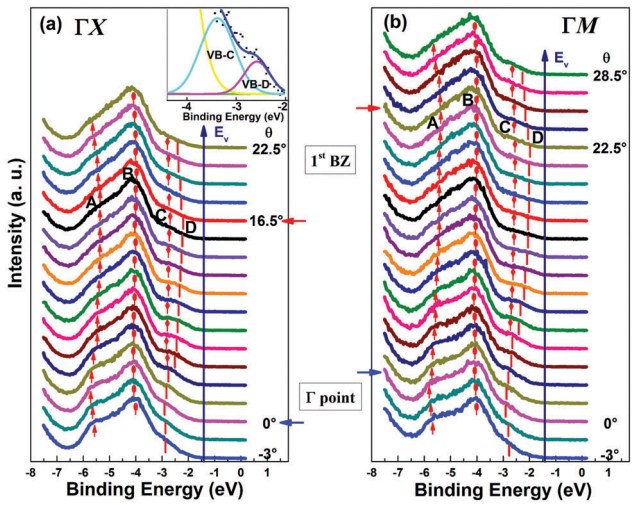

Fig. 3 (a) Angle-resolved energy distribution curves measured along ΓX; (b) the same, but measured along ΓM. The four VB peaks are denoted by arrows and bars. The inset shows the detailed fitting of VB-C and VB-D peaks.

respectively. This minimal position corresponds to the boundary of the first Brillouin zone (BZ) in each direction. However, the shifts are not identical, which are somewhat stronger along the ΓM direction, being 0.41 eV, 0.18 eV, 0.20 eV, and 0.73 eV for VB-A, VB-B, VB-C, and VB-D in the ΓX direction; and 0.48 eV, 0.18 eV, 0.40 eV and 0.98 eV in the ΓM direction, respectively. As θ increases beyond the 1st BZ boundary, all the peaks start to shift back towards higher BE again. These results indicate the symmetry around the BZ boundaries, as well as the Γ point.

The photon energy $h\nu$ was fixed at 21.22 eV. By adjusting the electron emission angle (θ), the band dispersions $E(\boldsymbol{k})$ could be obtained simply from the measured values of kinetic energy E_{kin} and the equation as follows:[36]

$$E_{\mathrm{kin}} = h\nu - \phi - |E_{\mathrm{B}}| \quad (1)$$

$$\hbar\boldsymbol{k}_{\parallel} = \sqrt{2mE_{\mathrm{kin}}} \times \sin\theta \quad (2)$$

$$\hbar\boldsymbol{k}_{\parallel} = [2m(h\nu - \Phi - |EB|)]^{\frac{1}{2}} \sin\theta \quad (3)$$

Here $\hbar\boldsymbol{k}_{\parallel}$ is the component parallel to the surface of the electron crystal momentum, Φ = 4.61 eV is the work function, and E_{B} is the binding energy.

Fig. 4 shows the energy dispersions of the four valence bands as a function of $\boldsymbol{k}_{\parallel}$ along ΓX and ΓM directions. By comparison, the 1st BZ boundary has a peak energy of ~−1.94 eV at the M point that is higher than ~−2.18 eV at the X point. The experimental results are consistent with the first-principles calculations, being ~−0.90 eV and ~−1.70 eV at the M point and the X point, respectively.[21] It suggests that the VB is a mixture of Pb-s and Br-p orbitals,[21,26] and the Br-p orbitals contribute mostly to the band features.[21,26] Interestingly, the VBM splits into two bands, VB-C and VB-D, at about $\boldsymbol{k}_{\parallel}$ = 0.14 Å^{-1} and ~0.24 Å^{-1} for ΓX and ΓM directions, respectively. This band splitting could be explained by comparing with the DFT results from the study of Jishi *et al.*[21] From the calculation, it is found that the bandgap of the cubic $CH_3NH_3PbBr_3$ single crystal is 2.23 eV and occurs at point R (1/2, 1/2, 1/2) in the BZ. Again, since the crystal could not be cleaved along the ΓR direction, we were unable to compare the VBM dispersions in this direction. However, the VBM dispersion in the ΓX direction is ~0.56 eV, which is smaller than the measured one of 0.73 eV as shown in Fig. 4(a). The VBM dispersion in the ΓM direction is ~1.45 eV,

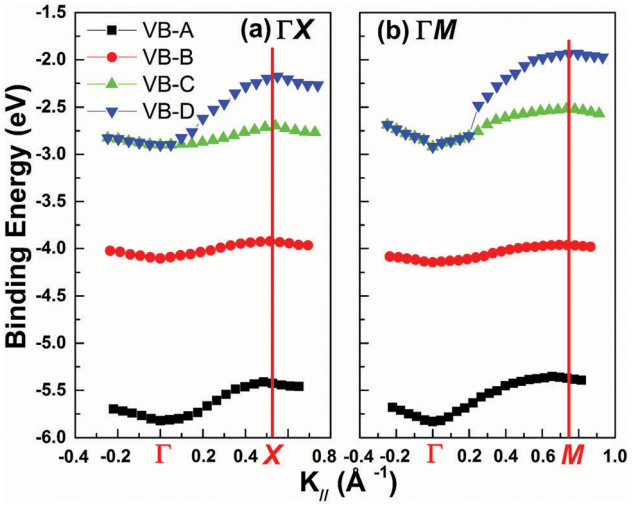

Fig. 4 Dispersions of the four valence bands of the $CH_3NH_3PbBr_3$ single crystal along (a) ΓX and (b) ΓM directions. The red lines denote the first BZ boundaries.

which is larger than the measured value of 0.98 eV as shown in Fig. 4(b). According to the band structure calculation, the second and third valence bands are very close to each other, and almost have the same value as the VBM in the vicinity of the Γ point in both directions. The average dispersions of the two bands are $\sim$0.14 eV and $\sim$0.2 eV, which are comparable with 0.20 eV and 0.40 eV of VB-C in ΓX and ΓM directions, respectively. Therefore, these two bands may contribute to the VB-C, and share the same $\boldsymbol{k}_{\parallel}$ value as VB-D near the Γ point.

Noticeably, the $\boldsymbol{k}_{\parallel}$ value at the X point is $\sim$0.53 Å^{-1} given by

$$\boldsymbol{k}_{\parallel} = \frac{\pi}{a} = 0.53 \text{ Å}^{-1} \quad (4)$$

for the lattice parameter a of 5.93 Å.[37,38] The $\boldsymbol{k}_{\parallel}$ value at the M point is $\sim$0.75 Å^{-1}. These calculated $\boldsymbol{k}_{\parallel}$ values are in good agreement with the measured results in Fig. 4.

The measured band dispersions are the key factors to understand the transport characteristics of perovskite single crystals. Under the one-dimensional tight-binding approximation, the energy dispersions were fitted by

$$E_B = E_C - 2t\cos(a\boldsymbol{k}_{\parallel}) \quad (5)$$

where E_C is the binding energy of the band center, t is the transfer integral, and a is the lattice spacing. From the formulation, t is estimated to be 0.18 eV for the VB-D curve in the ΓX direction. The effective hole mass m_h* in the VB region is given by

$$m_h^* = \frac{\hbar^2}{2ta^2} \quad (6)$$

Thus, the effective mass of the VB-D band in the ΓX direction is derived to be $0.59m_0$ (m_0 is the free electron mass). In a broad band model, where the band width W is much larger than k_BT (26 meV), the lower limit drift mobility of the hole is estimated to be 33.90 cm^2 V^{-1} s^{-1} according to the equation:[39]

$$\mu_h > 20\frac{m_0}{m_h^*} \times \frac{300}{T} \quad (7)$$

The calculated value of the hole mobility is comparable with some reports with values ranging from 19.4 to 56.1 cm^2 V^{-1} s^{-1} by photoluminescence measurements,[40] and 24.0 cm^2 V^{-1} s^{-1} from dark current–voltage measurements.[41] Other results such as 217 cm^2 V^{-1} s^{-1} and 206 cm^2 V^{-1} s^{-1} from time-of-flight measurements[5] are larger than the value we measured. Shi *et al.*[32] measured the mobility of the same sample using two methods, being 20 to 60 cm^2 V^{-1} s^{-1} by Hall effect measurements and 115 cm^2 V^{-1} s^{-1} by time-of-flight (TOF) measurements. The reason that the results from TOF measurements are higher than those from other methods is that there is a distribution of mobility, while TOF measurements give the mobility of carriers with the highest mobility. On the other hand, the DFT results showed that the ΓR direction should have the largest VBM dispersion, and thus lead to the lowest effective mass and highest hole mobility. Due to the limitation of the cleaving technique, we could not measure the dispersions along this direction, and may obtain a smaller hole mobility than expected as a result. It is also possible that the structure of the perovskite single crystal may be too complicated to be fully presented by the tight-binding approximation fitting, thus underestimating the hole mobility.

Niesner *et al.* discovered the giant Rashba splitting in $CH_3NH_3PbBr_3$ single crystals and confirmed the strong spin–orbit coupling (SOC) in both orthorhombic and cubic phases.[42] Normally, the presence of SOC is stronger in the conduction band than in the valence band.[21,43,44] However, due to the angle resolution of our facility, we did not observe clear Rashba splitting around the VBM or its effect on the largest band dispersions in both ΓX and ΓM directions. Our findings revealed the lower limit drift mobility of the holes in perovskite single crystals. In practical cases, the transport behavior of the real devices may be more complicated due to the interfacial characteristics between perovskite and other layers. The effective mass and carrier mobility would also be important for a fair evaluation of the possibility to use the perovskite material as a future channel material in field effect transistors for high speed performances.

Conclusions

In summary, we have studied the electronic structure of the cubic perovskite single crystal (001) surface using ARPES and IPES. The high quality of the smooth surface was confirmed by AFM and SEM. The elemental composition was investigated by XPS with a ratio close to the ideal value. Highly reproducible dispersive features of valence bands were observed with symmetry at the BZ center and boundaries. The four VB peaks are composed of Pb-s and Br-p orbitals as theoretical models predicted, and had different band dispersion widths. The largest dispersion came from the lowest binding energy band, being $\sim$0.73 eV and $\sim$0.98 eV for ΓX and ΓM directions, respectively. The measured band dispersions correspond to an effective hole mass of $\sim 0.59m_0$ and a lower limit of the hole mobility of 33.90 cm^2 V^{-1} s^{-1} from the tight-binding fitting.

Acknowledgements

The authors would like to thank the financial support from National Science Foundation (Grant No. CBET-1437656 and DMR-1303742). Huang acknowledges the financial support from National Science Foundation under the award of OIA-1538893. Meng was supported by China 1000-Young Talents Plan and the National Natural Science Foundation of China Grant (11574402, 51502351). Technical support from the Nanocenter in the University of Rochester is highly appreciated.

References

1 A. Kojima, K. Teshima, Y. Shirai and T. Miyasaka, *J. Am. Chem. Soc.*, 2009, **131**, 6050–6051.
2 H. J. Snaith, *J. Phys. Chem. Lett.*, 2013, **4**, 3623–3630.
3 C. Grätzel and S. M. Zakeeruddin, *Mater. Today*, 2013, **16**, 11–18.
4 C. Bi, Y. Shao, Y. Yuan, Z. Xiao, C. Wang, Y. Gao and J. Huang, *J. Mater. Chem. A*, 2014, **2**, 18508–18514.
5 H. Wei, Y. Fang, P. Mulligan, W. Chuirazzi, H.-H. Fang, C. Wang, B. R. Ecker, Y. Gao, M. A. Loi and L. Cao, *Nat. Photonics*, 2016, **10**, 333–339.
6 National Renewable Energy Laboratory Best Research-Cell Efficiencies, www.nrel.gov/ncpv/images/efficiency_chart.jpg, accessed 8, Jan, 2017.
7 Z.-K. Tan, R. S. Moghaddam, M. L. Lai, P. Docampo, R. Higler, F. Deschler, M. Price, A. Sadhanala, L. M. Pazos and D. Credgington, *Nat. Nanotechnol.*, 2014, **9**, 687–692.
8 F. Deschler, M. Price, S. Pathak, L. E. Klintberg, D.-D. Jarausch, R. Higler, S. Hüttner, T. Leijtens, S. D. Stranks and H. J. Snaith, *J. Phys. Chem. Lett.*, 2014, **5**, 1421–1426.
9 Y. Li, X. Xu, C. Wang, C. Wang, F. Xie, J. Yang and Y. Gao, *AIP Adv.*, 2015, **5**, 097111.
10 Z. Xiao, C. Bi, Y. Shao, Q. Dong, Q. Wang, Y. Yuan, C. Wang, Y. Gao and J. Huang, *Energy Environ. Sci.*, 2014, **7**, 2619–2623.
11 S. D. Stranks and H. J. Snaith, *Nat. Nanotechnol.*, 2015, **10**, 391–402.
12 Y. Wang, Y. Shi, G. Xin, J. Lian and J. Shi, *Cryst. Growth Des.*, 2015, **15**, 4741–4749.
13 X. Liu, C. Wang, L. Lyu, C. Wang, Z. Xiao, C. Bi, J. Huang and Y. Gao, *Phys. Chem. Chem. Phys.*, 2015, **17**, 896–902.
14 C. Wang, C. Wang, X. Liu, J. Kauppi, Y. Shao, Z. Xiao, C. Bi, J. Huang and Y. Gao, *Appl. Phys. Lett.*, 2015, **106**, 111603.
15 C. Wang, X. Liu, C. Wang, Z. Xiao, C. Bi, Y. Shao, J. Huang and Y. Gao, *J. Vac. Sci. Technol., B: Nanotechnol. Microelectron.: Mater., Process., Meas., Phenom.*, 2015, **33**, 032401.
16 Y. Li, X. Xu, C. Wang, C. Wang, F. Xie, J. Yang and Y. Gao, *J. Phys. Chem. C*, 2015, **119**, 23996–24002.
17 C. Wang, Y. Li, X. Xu, C. Wang, F. Xie and Y. Gao, *Chem. Phys. Lett.*, 2016, **649**, 151–155.
18 G. Niu, W. Li, F. Meng, L. Wang, H. Dong and Y. Qiu, *J. Mater. Chem. A*, 2014, **2**, 705–710.
19 J. M. Frost, K. T. Butler, F. Brivio, C. H. Hendon, M. Van Schilfgaarde and A. Walsh, *Nano Lett.*, 2014, **14**, 2584–2590.
20 X. Y. Chin, D. Cortecchia, J. Yin, A. Bruno and C. Soci, *Nat. Commun.*, 2015, **6**, 7383.
21 R. A. Jishi, O. B. Ta and A. A. Sharif, *J. Phys. Chem. C*, 2014, **118**, 28344–28349.
22 A. M. Leguy, P. Azarhoosh, M. I. Alonso, M. Campoy-Quiles, O. J. Weber, J. Yao, D. Bryant, M. T. Weller, J. Nelson and A. Walsh, *Nanoscale*, 2016, **8**, 6317–6327.
23 R. Lindblad, N. K. Jena, B. Philippe, J. Oscarsson, D. Bi, A. Lindblad, S. Mandal, B. Pal, D. D. Sarma and O. Karis, *J. Phys. Chem. C*, 2015, **119**, 1818–1825.
24 F. Brivio, J. M. Frost, J. M. Skelton, A. J. Jackson, O. J. Weber, M. T. Weller, A. R. Goni, A. M. Leguy, P. R. Barnes and A. Walsh, *Phys. Rev. B: Condens. Matter Mater. Phys.*, 2015, **92**, 144308.
25 A. D. Wright, C. Verdi, R. L. Milot, G. E. Eperon, M. A. Pérez-Osorio, H. J. Snaith, F. Giustino, M. B. Johnston and L. M. Herz, *Nat. Commun.*, 2016, **7**, 11755.
26 J.-S. Park, S. Choi, Y. Yan, Y. Yang, J. M. Luther, S.-H. Wei, P. Parilla and K. Zhu, *J. Phys. Chem. Lett.*, 2015, **6**, 4304–4308.
27 J. Even, L. Pedesseau, J.-M. Jancu and C. Katan, *J. Phys. Chem. Lett.*, 2013, **4**, 2999–3005.
28 F. Brivio, A. B. Walker and A. Walsh, *APL Mater.*, 2013, **1**, 042111.
29 X. Liu, C. Wang, C. Wang, I. Irfan and Y. Gao, *Org. Electron.*, 2015, **17**, 325–333.
30 X. Liu, S. Yi, C. Wang, C. Wang and Y. Gao, *J. Appl. Phys.*, 2014, **115**, 163708.
31 C. Wang, X. Liu, C. Wang, X. Xu, Y. Li, F. Xie and Y. Gao, *Appl. Phys. Lett.*, 2015, **106**, 121603.
32 D. Shi, V. Adinolfi, R. Comin, M. Yuan, E. Alarousu, A. Buin, Y. Chen, S. Hoogland, A. Rothenberger and K. Katsiev, *Science*, 2015, **347**, 519–522.
33 N. Kedem, T. M. Brenner, M. Kulbak, N. Schaefer, S. Levcenko, I. Levine, D. Abou-Ras, G. Hodes and D. Cahen, *J. Phys. Chem. Lett.*, 2015, **6**, 2469–2476.
34 Y. Gao, *Mater. Sci. Eng., R*, 2010, **68**, 39–87.
35 E. M. Hutter, M. C. Gélvez-Rueda, A. Osherov, V. Bulović, F. C. Grozema, S. D. Stranks and T. J. Savenije, *Nat. Mater.*, 2017, **16**, 115–120.
36 T.-C. Chiang, J. Knapp, M. Aono and D. Eastman, *Phys. Rev. B: Condens. Matter Mater. Phys.*, 1980, **21**, 3513.
37 Y. Liu, Z. Yang, D. Cui, X. Ren, J. Sun, X. Liu, J. Zhang, Q. Wei, H. Fan and F. Yu, *Adv. Mater.*, 2015, **27**, 5176–5183.
38 H. Mashiyama, Y. Kawamura, E. Magome and Y. Kubota, *J. Korean Phys. Soc.*, 2003, **42**, S1026–S1029.
39 H. Fröhlich and G. Sewell, *Proc. Phys. Soc.*, 1959, **74**, 643.
40 W. Tian, C. Zhao, J. Leng, R. Cui and S. Jin, *J. Am. Chem. Soc.*, 2015, **137**, 12458–12461.
41 M. I. Saidaminov, A. L. Abdelhady, B. Murali, E. Alarousu, V. M. Burlakov, W. Peng, I. Dursun, L. Wang, Y. He and G. Maculan, *Nat. Commun.*, 2015, **6**, 7586.
42 D. Niesner, M. Wilhelm, I. Levchuk, A. Osvet, S. Shrestha, M. Batentschuk, C. Brabec and T. Fauster, *Phys. Rev. Lett.*, 2016, **117**, 126401.
43 T. Etienne, E. Mosconi and F. De Angelis, *J. Phys. Chem. Lett.*, 2016, **7**, 1638–1645.
44 A. Amat, E. Mosconi, E. Ronca, C. Quarti, P. Umari, M. K. Nazeeruddin, M. Grätzel and F. De Angelis, *Nano Lett.*, 2014, **14**, 3608–3616.